Analysis of Sea Clutter with a Dual-Band Photonics-based Coherent Radar Network

Salvatore Maresca
CNR
IEIIT Institute
Pisa, Italy
salvatore.maresca@cnr.it

Filippo Scotti
CNIT
PNTLab Institute
Pisa, Italy
filippo.scotti@cnit.it

Malik M. H. Amir
SSSA
TeCIP Institute
Pisa, Italy
malikmuhammadharis.amir@santannapisa.it

Gaurav Pandey
SSSA
TeCIP Institute
Pisa, Italy
gaurav.pandey@santannapisa.it

Antonio Malacarne
CNIT
PNTLab Institute
Pisa, Italy
antonio.malacarne@cnit.it

Mirco Scaffardi
CNIT
PNTLab Institute
Pisa, Italy
antonio.malacarne@cnit.it

Paolo Ghelfi
CNIT
PNTLab Institute
Pisa, Italy
paolo.ghelfi@cnit.it

Antonella Bogoni
CNIT
PNTLab Institute
Pisa, Italy
antonella.bogoni@cnit.it

OCEANS 2023 - Limerick | 979-8-3503-3226-1/23/$31.00 ©2023 IEEE | DOI: 10.1109/OCEANSLimerick52467.2023.10244616

***Abstract*—Microwave photonics has the potential to allow the realization of coherent multiple-input multiple-output (MIMO) radar networks with widely distributed antennas, thanks to the inherent coherence of photonics systems, and to the broadband, low-distortion, and interference-immune optical signal distribution.**

Recently, the first dual-band photonics-based coherent MIMO radar has been presented. The system, designed to operate in a real port for maritime traffic monitoring, has been integrated within the monitoring and control application (MoniCA) platform of the Port of Livorno, Italy, thus enabling the fusion of the radar data with other types of data managed by the multi-service MoniCA platform.

This paper describes the statistical analysis performed on signals back-scattered from the sea and recorded by the photonics-based radar network. The statistical analysis of data shows that, under specific experimental and sea state conditions, the Rayleigh model fits well the signal amplitude distribution, thus easing the mathematical tractability of the target detection problem.

***Index Terms*—Sea clutter, statistical analysis, MIMO radar, maritime surveillance, port infrastructure, microwave photonics.**

I. Introduction

This paper deals with the statistical analysis of sea clutter using signals acquired by a coherent network of dual-band radars based on photonic technology and deployed in a real operative maritime surveillance scenario.

Multiple radars distributed in space, by overcoming the traditional notion of stand-alone, local radar, have led to the definition of the concept of radar network [1]. Distributed radar networks are systems in which each node can receive the echoes coming from signals transmitted by the other nodes in the network. This kind of network topology has become famous under the name of multi-input multi-output (MIMO) radar [2], for its strong similarities with the world of MIMO communication systems.

In this context, photonic technology has demonstrated to grant great flexibility to radar systems [3], enabling them to transmit and receive signals from different sites, but also to simultaneously handle different waveforms on different radio frequency (RF) carriers. Thus, photonics-assisted generation, distribution, and reception of RF signals potentially allow for high signal stability and phase synchronization among the MIMO radar network peripherals.

Recently, a photonics-based MIMO radar network exploiting coherent and dual-band signals has been presented for the first time in [4]. The system is deployed in the port of Livorno, Italy, one of the major freight ports in the European Union. By exploiting the available fiber network infrastructure, the radar peripherals (RPs), i.e., transmit/receive nodes, have been remoted for a better observation of the maritime traffic. As sketched in Fig. 1, the full system architecture is composed by three RPs connected via optical fiber links to a central unit (CU). The system transmits in two RF bands (i.e., S and X). In [4], the benefit of geometric and frequency diversities on the target detection and localization has been discussed, demonstrating the fundamental importance of centralized processing and data coherence granted by such system.

Moreover, the integration of the MIMO radar functionality with the existing port multi-service monitoring and control application (MoniCA) platform has been reported in [5], where the radar tracks have been associated to the automatic identification system (AIS) navigation information made available by MoniCA. Finally, preliminary results of inverse synthetic aperture radar (ISAR) imaging have been presented in [6].

In this paper, closely following the analysis in [7]–[10] and [11], [13], the statistical properties of sea clutter are analyzed. Monostatic and bistatic radar configurations at both S- and X-bands are taken into account. On one hand, the principal aim of this analysis is to start outlining the effect of both

This research is partially funded within the projects COSMOS by the FISR funding scheme, Italian Ministry of University and Research, grant number FISR2019_03476, CLARIFIER (SPS funding scheme by NATO), ESTIMATOR and O'CLOCK (both funded by U.S.A. Office of Naval Research Global).

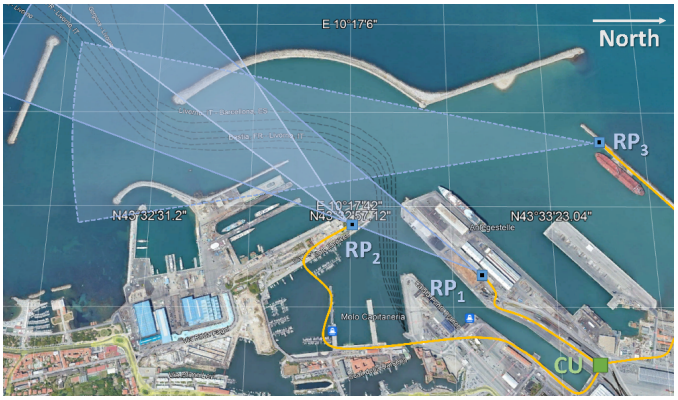

Fig. 1. Topology of the MIMO radar network in the port of Livorno for traffic monitoring. The system central unit (CU) is connected to the radar peripherals (RPs) with optical fiber (represented by light-blue lines). The CU and the RPs are represented by the green and blue squares, respectively. The light-blue shadowed areas schematically depict the transmission pattern of the employed antennas. Fiber links are depicted by the orange curves.

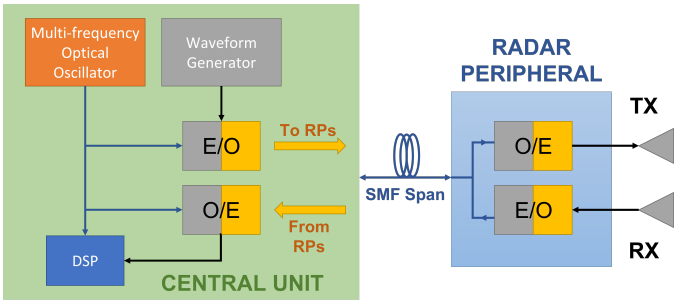

Fig. 2. High-level photonics-based coherent radar network architecture. DSP: digital signal processing; RP: radar peripheral; E/O: electro-optical; O/E: opto-electrical; TX: transmitter; RX: receiver; SMF: single-mode fiber.

geometric and frequency diversities on sea clutter characteristics, for enhancing the overall target detection performance of the proposed system under any operative condition. On the other hand, the proposed system and methodology may result precious also for supporting remote sea state sensing, which continues to attract significant interest in the scientific community [14].

The remainder of the paper is organized as follows. In Section II, the photonics-based radar network is presented. The mathematical guidelines for the statistical analysis of data are given in Section III, whereas results of the statistical analysis are presented in Section IV. Finally, conclusions and perspectives are given in Section V.

II. Photonics-based Radar Network

The photonics-based radar network in the Port of Livorno is actually composed of three nodes: a CU and two remoted RPs working simultaneously in the S- and X-bands. As depicted in Fig. 1, the complete system also includes a third RP, which at present is installed but not yet operative.

In Fig. 1, the CU is represented by a green square, whereas the sites of RP_1 and RP_2 and their areas of coverage are depicted by the blue squares and light-blue shadowed areas, respectively. The area of coverage that will be granted by RP_3 is depicted by a light-blue shadowed area with dashed contour. The current geometry of RP_1 and RP_2 allows to cover a common area of observation with some angular diversity. In fact, the angle subtended by the illumination directions of RP_1 and RP_2 is about $40°$. The activation of RP_3 will increase the overall angular diversity of the system and further extend the monitored area, as shown in Fig. 1.

The MIMO network nodes are connected by means of optical single-mode fibers (SMFs). Through these links, the CU sends the signals to be transmitted to the RPs, whereas the RPs, in turn, send the received signals back to the CU for acquisition, digitization and processing.

Currently, the presented system is set to observe the southern entrance of the port, with the aim of providing all-day all-time capability to monitor the maritime traffic with the sensitivity and resolution to detect even small boats [6]. Nevertheless, the antennas at the RPs can be arbitrarily oriented to cover the desired area inside or outside the port.

A. System Architecture

The high-level scheme of the system architecture is depicted in Fig. 2. The main component of the CU is the multi-frequency optical oscillator (i.e., the master clock), fed to an E/O block to implement the conversion to the optical domain of the intermediate-frequency (IF) radar signal at the output of the electrical waveform generator. Thanks to an optical SMF link, the obtained optical signal is routed to the remoted RPs.

At the RP, a dual O/E stage converts the signal back into the RF domain, at the same time operating the up-conversion of the IF signal to multiple RF frequencies [5], [6]. Then, at the TX side of the RF front-end, the O/E converted signal is transmitted towards the monitored area. At the RX side, all the radar echoes back-scattered from the observed scene (e.g., targets, clutter) are received by the RP. In reception, again, an E/O block converts the RF received signal to the optical domain to send it back to the CU over SMF link.

At the CU, an O/E block takes the signal back to the electrical domain, at the same time operating the down-conversion of the RF signal to IF for acquisition by an analog-to-digital converter (ADC) and further processing.

B. System Parameters

During the acqusition tests, conducted on July 23, 2021, the photonics-based MIMO radar worked in a reduced system configuration, with only RP_1 and RP_2 operating on both S and X bands, see Fig. 1. The exact coordinates of the three RPs, along with the pointing directions (clockwise from North) of their antennas are summarized in Table I, whereas the main system operational parameters are reported in Table II.

Each RP is equipped with two horn antennas, one for transmitting/receiving at S-band and one for transmitting/receiving at X-band. As described in Table II, the antenna aperture is $18°$ at both frequencies. This means that, although the excellent range resolution achieved by the system (i.e., 1.5 m),

Fig. 3. Pictures of the two reference targets: a) 4.5 m long cooperative fiberglass speedboat, carrying a GPS receiver for ground-truth recording; b) 225 m long non-cooperative ferry. For this target, the distance between the radar mast and the funnel is approximately 110 m.

the azimuth resolution of each RP is quite coarse. This feature, associated with a monitored area enclosed between breakwater walls, piers and other man-made structures, see Fig. 1, inevitably leads to collect not only echoes from the sea surface, but also from static targets as well. In this sense, future on-field acquisitions with the complete system will be conducted by pointing the RP antennas outside the port area.

C. System Operation

For the on-field validation of the system detection and imaging capabilities, two different types of targets have been considered in [6]: a 4.5 m length cooperative fiberglass speedboat with an electromagnetic radar cross section (RCS) of roughly 1 m^2, and a ferry of 225 m length. For completeness, pictures of the two types of targets are given in Fig. 3.

The first target (i.e., the speedboat), see Fig. 3 a), has been considered for evaluating the detection and tracking effectiveness of the system against targets with very small RCS. During the repetitions of the test, the boat followed different trajectories, recorded into global positioning system (GPS) logs. Instead, the second target (i.e., the ferry), see Fig. 3 b), has been used for assessing the system imaging capabilities. The interested reader may find the necessary information in [6].

TABLE I
RPs Coordinates and Antennas Pointing Directions

Parameter	RP_1	RP_2	RP_3
Longitude	10°17′50.1″ E	10°17′45.3″ E	10°17′29.6″ E
Latitude	43°33′11.2″ N	43°32′57.3″ N	43°33′30.1″ N
Dir. vs North	200°	240°	180° (est.)

TABLE II
Setup Parameters of the Photonics-Based MIMO Radar

Parameter	Value/Description
No. of TXs	2(3)
No. of RXs	2(3)
Signal Waveform	Lin. Freq. Mod. (LFM) Chirp
S-band Carrier Frequency	2.9 GHz
X-band Carrier Frequency	9.7 GHz
Intermediate Frequency	100 MHz
Pulse duration	100 ns ÷ 5 μs
Chirp Bandwidth	100 MHz
Pulse Repetition Interval	50 μs
Output Power per antenna	10 W (40 dBm)
Sampling Frequency	400 MHz
Antenna Gain/Aperture	20 dBi/ $\sim 18°$
Noise Figure (NF)	6 dB /17 dB (S-/X-band)
Sensitivity	−103 dBm / − 110 dBm (S-/X-band)

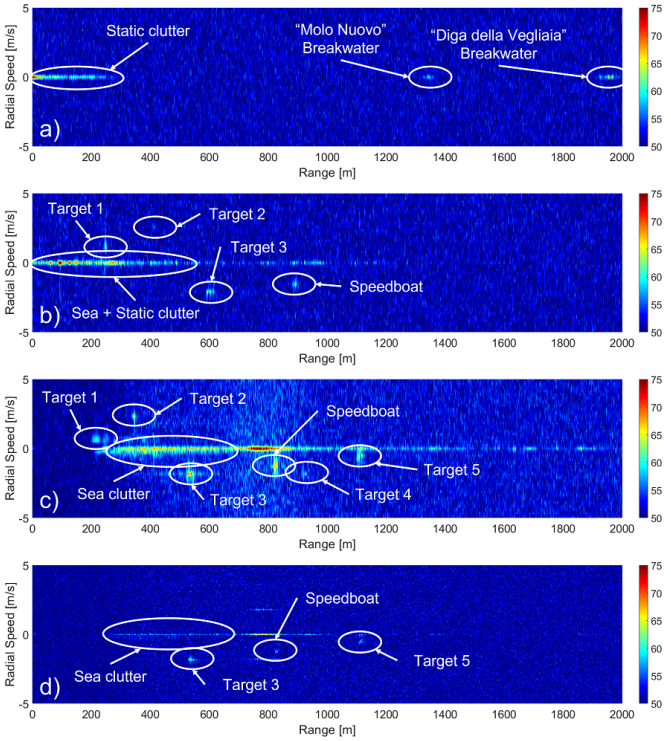

Fig. 4. Exemplary case of a MIMO system data acquisition. The cross-correlation maps are depicted at the varying of range and radial speed for the following channels of the system: a) TX_1-RX_1 at S-band, b) TX_2-RX_1 at S-band, d) TX_2-RX_2 at S-band, e) TX_2-RX_2 at X-band.

In this paper, the cross-correlation maps for the employed radar channels are evaluated at the varying of range and radial speed. With 2 TXs and 2 RXs available for each band, the system can process the acquired signals and extrapolate 4 range/velocity maps for each band, considering all the combinations of TX and RX in the two RPs. For clarity, the maps have been limited between 2000 m range and ± 5 m/s (i.e., $\approx \pm 10$ kn) along the radial speed dimensions. Four sample range-velocity maps are reported in Fig. 4.

In the plots, the resolution in range is 1.5 m and it is equal for the two bands, since depending on the signal bandwidth, which is 100 MHz for both S- and X-bands. Instead, the resolution in velocity for the X-band is about three times better than for the S-band, given the proportionality ratio between the two RF wavelengths. It is important to observe that, in the four subplots of Fig. 4, the position and radial velocity of the scatterers in the maps are not coincident, due to the different target-sensor geometries provided by all the TX-RX combinations.

The range-velocity map for the monostatic S-band channel formed by the TX_1 and RX_1 of RP_1 is shown in Fig. 4 a). During the tests, RP_1 has demonstrated a poor illumination capability of the internal area of the port. In fact, it is possible to observe only stationary clutter extending up to about 250 m range and two less pronounced peaks at about 1340 m and 1955 m, corresponding to the distances of the two lighthouses at the two breakwaters, i.e., "Molo Nuovo" and "Diga della

Vegliaia" respectively. The same two peaks, but less evident, are present in the X-band case, not reported here. The reasons of this degradation may be found not only in the larger free-space attenuation in the X-band, but probably also in the higher gain of the S-band front-ends with respect to the X-band.

The range-velocity map for the bistatic S-band channel formed by TX_2 and RX_1 is depicted in Fig. 4 b). In this case, TX_2 has demonstrated a better illumination capability of the internal area of the port, thus manifesting a better target detection performance. In fact, in Fig. 4 b) three moving targets are detected in addition to the speedboat. Sea clutter returns and echoes from stationary structures can be observed extending up to ≈ 500 m.

As already mentioned, the analysis of RP_2 has demonstrated a better target detection capability than RP_1 in monitoring the internal area of the port, accompanied by an increased sensitivity also to sea clutter returns. In fact, as it is possible to observe in Fig. 4 c), five targets can be detected, in addition to the speedboat. However, since the antenna illuminates a large portion of the first breakwater arc, echoes from stationary structures often mix with sea clutter returns over a large range interval between about 215 and 1865 m.

Finally, sea clutter can be observed between 205 and 445 m, with returns extending in the radial speed interval ± 1 m/s. The speedboat, as well as the third and fifth targets are still detectable in Fig. 4 d), whereas the first, second and forth targets are immersed in the noise floor. Instead, an additional return is visible at about 785 m and -1.81 m/s. This peak is most probably an artifact caused by the amplifier saturation when strong stationary targets are illuminated. Thus, replicas of the stationary peak appear along the radial speed component. This phenomenon deserves further investigation to be properly mitigated.

The analysis of the bistatic channels formed by TX_1 and RX_2 has not been reported, due to the poor illumination capability of by TX_1 inside the port, affecting also the signals received by RX_2. As mentioned, to illuminate range cells containing only sea clutter echoes, future acquisitions will be conducted by pointing the RP antennas outside the port area.

III. Statistical Analysis of Data

The analysis of data live-recorded by the photonics-based radar network can be divided into statistical and spectral analyses, as described in [11], [12]. Focusing on the first type of analysis, this paper provides a detailed study of sea clutter characteristics observed by all the MIMO radar channels (i.e., both monostatic and bistatic), at both S- and X-band.

Before any further processing, a preliminary analysis has been carried out on the data, with the final purpose of evaluating the correct balance between the in-phase (I) and quadrature (Q) signal components. However, results of this analysis have been omitted for conciseness.

A. Non-Gaussianity Analysis

The Central Limit Theorem (CLT) applies when the number of scatterers from a given illuminated surface is large enough. In this case, clutter is a complex Gaussian process, meaning that its amplitude is Rayleigh distributed.

For this very reason, it is of paramount importance to study the probability density functions (PDFs) of both the I and Q components and check whether they are Gaussian distributed. To simplify this analysis, two parameters can be preliminarily evaluated. These parameters are the *skewness* and *kurtosis* coefficients, which describe how a given random real-valued variable deviates from being Gaussian distributed.

By denoting with Z the generic real-valued random variable, skewness, i.e., $S(Z)$, and kurtosis, i.e., $K(Z)$, are defined as:

$$S(Z) \triangleq \frac{E\{(Z - E\{Z\})^3\}}{E^{3/2}\{(Z - E\{Z\})^2\}}, \tag{1}$$

$$K(Z) \triangleq \frac{E\{(Z - E\{Z\})^4\}}{E^{2}\{(Z - E\{Z\})^2\}}, \tag{2}$$

where $E\{.\}$ is the expectation operator.

Skewness provides information about the symmetry of the PDF around its mean value. A negative (positive) value corresponds to a distribution with an asymmetric tail extending to the left (right) of the mean value.

Kurtosis measures instead the relative peakedness (if negative) or flatness (if positive) of the distribution relative to the Gaussian PDF. For a Gaussian distribution, $S(Z) = 0$ and $K(Z) = 3$ [13].

B. Amplitude Modelling

The successive step of this analysis consists in evaluating the empirical distribution of the received signal amplitude, and then in comparing it with a series of well-known models. These models, i.e., the Rayleigh (R), Log-normal (LN), Weibull (W), are commonly used to fit the amplitude PDF (APDF) of heavy-tailed non Gaussian X-band sea clutter [13]. Moreover, they have been successfully applied for modelling data at other frequencies [11], [12]. The analytical expressions of these PDFs and their moments are reported below.

1) Rayleigh Model: By denoting with $R = |Z_I + jZ_Q|$ the clutter signal amplitude, with Z_I and Z_Q respectively the *I* and *Q* components of the signal, the expressions of the Rayleigh distribution and its moments are given by:

$$p_R(r) = \frac{2r}{\lambda^2} \exp\{-(r/\lambda)^2\} u(r), \tag{3}$$

$$E\{R^n\} = \lambda^n \cdot \Gamma(n/2 + 1), \tag{4}$$

where λ is the scale parameter, $\Gamma(r)$ is the gamma function with input argument r, and $u(r)$ is the unit step function, which is 0 for $r < 0$ and 1 for $r \geq 0$.

2) Weibull Model: The expressions of the Weibull distribution and its moments are given by:

$$p_R(r) = \frac{c}{b^c} r^{c-1} \exp\{-(r/b)^c\} u(r), \tag{5}$$

$$E\{R^n\} = b^n \cdot \Gamma(n/c + 1), \tag{6}$$

where c is the shape parameter, b is the scale parameter. It is worth noticing that the Weibull clutter model coincides with the Rayleigh model when $c = 2$.

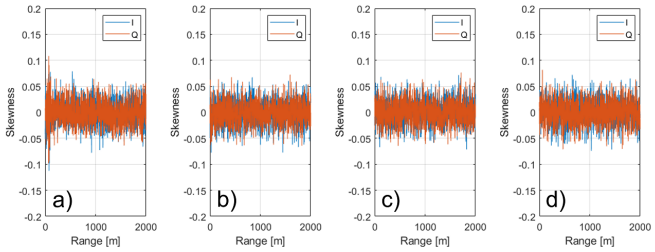

Fig. 5. Analysis of skewness coefficient versus range: a) TX_1-RX_1 at S-band, b) TX_2-RX_1 at S-band, c) TX_2-RX_2 at S-band, d) TX_2-RX_2 at X-band.

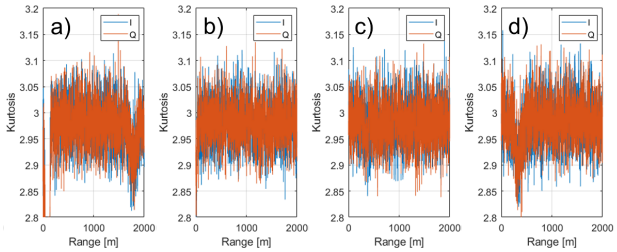

Fig. 6. Analysis of kurtosis coefficient versus range: a) TX_1-RX_1 at S-band, b) TX_2-RX_1 at S-band, c) TX_2-RX_2 at S-band, d) TX_2-RX_2 at X-band.

3) Log-Normal Model: The expressions of the Log-Normal PDF and its moments are given by:

$$p_R(r) = \frac{1}{r\sqrt{2\pi\sigma^2}} \exp\left\{-\frac{1}{2\sigma^2}\left[(\ln r - \ln \delta)^2\right]\right\} u(r), \quad (7)$$

$$E\{R^n\} \triangleq \delta^n \exp\{n^2\sigma^2/2\}, \quad (8)$$

where σ is the shape parameter, δ is the scale parameter and $u(r)$ is the unit step function.

IV. Experimental Results

A. Analysis of Skewness and Kurtosis

Skewness and kurtosis are estimated for the same radar channels displayed in Fig. 4 at the varying of range. Results are averaged over all the performed acquisitions. For each radar channel, both the I and Q signal components are considered.

The estimated skewness curves are depicted in Fig. 5. With the exception of few samples for the TX_1-RX_1 channel at S-band, see Fig. 5 a), all the observed radar channels show pretty good simmetry (i.e., $S(Z) \approx 0$) of the PDF around the mean value, with small fluctuations of about ± 0.05.

The estimated kurtosis curves are depicted in Fig. 6. Here, the PDFs of the I and Q signal components show strong peakedness in some specific intervals. In fact, in the case of TX_1-RX_1 at S-band, see Fig. 6 a), $K(Z) < 3$ up to 150 m (i.e., close to the pier) and around 1800 m (i.e., close to the second breakwater wall). Instead, no significant deviations from the Gaussian PDF are to be expected for TX_2-RX_1 channel at S-band, see Fig. 6 b), since $K(Z) \approx 3$.

In the case of TX_2-RX_2 channel, slightly different behaviours can be observed between the S- and X-bands. When this latter band is employed, the I and Q signal components show some peakedness around 325 m distance where $K(Z) \approx 2.8$, see Fig. 6 d). On the contrary, when the S-band is utilized, this peakedness almost disappears, see Fig. 6 c). For kurtosis, fluctuations are in the order of about ± 0.1.

These preliminary results suggest that the APDF of sea clutter inside the port, under very calm sea state conditions, is likely to be Rayleigh distributed. The following analysis is aimed at verifying this hypothesis.

B. Analysis of Scale and Shape Parameters

The characteristic parameters (i.e., scale and shape) of the three theoretical amplitude distribution models are estimated using the method of moments (MoM) [13] from the range profiles at the output of the matched filter. Curves are obtained from one of the files acquired on July 23, 2021. Results are calculated from 300 PRIs. Again, the same radar channels of Fig. 4 are considered.

1) Scale Parameters: The scale parameter λ of the Rayleigh distribution (blue line) is shown in Fig. 7. It is possible to observe different values among the four considered channels. Depending on the radar channel, the average value of $\log_{10}(\lambda)$ for sea clutter cells varies between 3.70, see Fig. 7 a) and 3.90, see Fig. 7 c). Considering the radar channel formed by TX_2 and RX_2, the average scale parameter value for sea clutter passes from 3.90 to 3.75, respectively for the S-band, see Fig. 7 c), and the X-band, see Fig. 7 d). Moreover, when static clutter (e.g., piers, breakwater walls, lighthouses, or other man-made structures) or large maritime targets are present, the estimated $\log_{10}(\lambda)$ increases to about 4.10, leading to a more heavy-tailed amplitude distribution.

The scale b parameter of the Weibull distribution is represented by the red line in Fig. 7. For this parameter, it is possible to draw similar comments to those done for the scale parameter of the Rayleigh distribution, except for the overall amplitude, which is slighlty larger. For the TX_2-RX_2 channel at S-band, see Fig. 7 c), both Rayleigh and Weibull distributions exhibit an evident arc between 500 and 1000 m. Its appearance may be motivated by the presence of sea clutter in the same interval, see Fig. 4 c). This arc almost disappears at X-band, see Fig. 7 d), probably due to the lower sensitivity of the system.

For completeness, the scale δ parameter of the Log-Normal distribution (yellow line) is depicted in Fig. 7, too. Its pattern along range follows the Rayleigh and Weibull distributions, but with values in log-10 scale of about 0.95.

2) Shape Parameters: As discussed is Section III, only the Weibull and Log-Normal dstributions are characterized by the shape parameter. Indeed, it is this parameter, namely c, that governs the similarity of the Weibull with the Rayleigh distribution. In fact, when $c = 2$, the Weibull coincides with the Rayleigh distribution.

As it is possible to observe in Fig. 8, in all the radar channels and for all the observed range cells, $c \approx 2$, with maximum

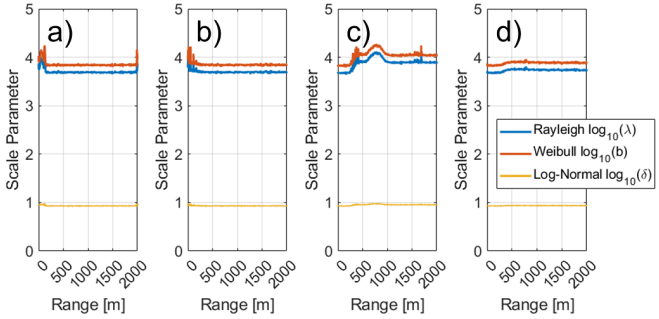

Fig. 7. Scale parameters of the Rayleigh (blue), Weibull (red) and Log-Normal (yellow) distributions: a) TX_1-RX_1 at S-band, b) TX_2-RX_1 at S-band, c) TX_2-RX_2 at S-band, d) TX_2-RX_2 at X-band.

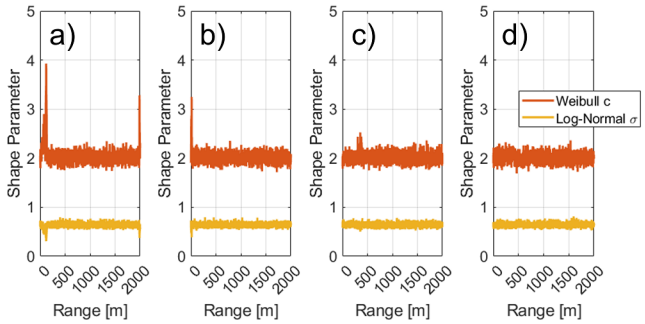

Fig. 8. Shape parameters of the Weibull (red) and Log-Normal (yellow) distributions: a) TX_1-RX_1 at S-band, b) TX_2-RX_1 at S-band, c) TX_2-RX_2 at S-band, d) TX_2-RX_2 at X-band.

fluctuations of about ± 0.2. This confirms the results obtained with the analysis of skewness and kurtosis coefficients. When the received signal contains not only sea clutter but also echoes from static targets, such as piers, breakwater walls, lighthouses and other man-made structures, then $c > 2$, meaning that the distribution is more peaked than the Rayleigh one [11].

For completeness, the shape parameter σ of the Log-Normal distribution is depicted in Fig. 8 as well. For the majority of range cells, the value varies around 0.65 with maximum fluctuations of about ± 0.1. This value becomes smaller before 150 m only for the TX_1-RX_1 channel at S-band, see Fig. 8 a). It is worth noticing that, as discussed in [13], the Log-Normal distribution does not belong to the family of compound-Gaussian (CG) models, thus complicating the definition of the proper target detection strategy.

C. Amplitude Modelling

The PDFs of the proposed mathematical models (i.e., Rayleigh, Weibull and Log-Normal) are evaluated from the scale and shape parameters estimated so far, at specific range cells of interest, and compared with the empirical amplitude distribution obtained from the histogram. In the following analysis, moments up to the sixth-order are also evaluated, to better evaluate the similarities of the proposed models with the distribution of the empirical data.

1) S-band Radar Channels: Two sample cases are reported for the S-band channels: *i)* TX_2-RX_2 monostatic radar observing range cell no. 1067, corresponding to ≈ 400 m distance; *ii) i)* TX_2-RX_1 bistatic radar illuminating range cell no. 2088, i.e., ≈ 783 m.

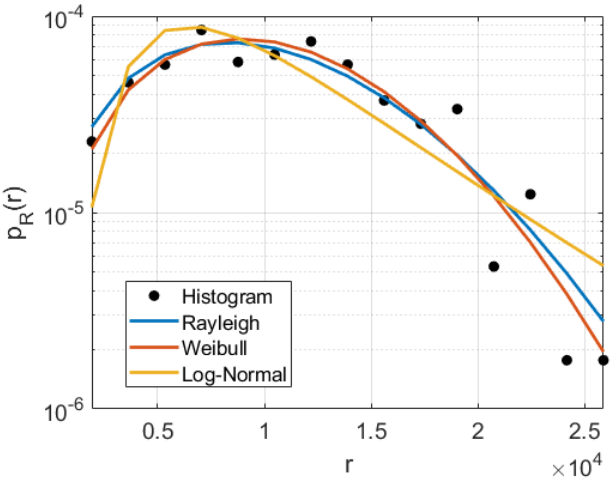

Fig. 9. Analysis of amplitude probability density functions (APDFs) for TX_2-RX_2 radar channel at S-band at range cell no. 1067 (i.e., ≈ 400 m).

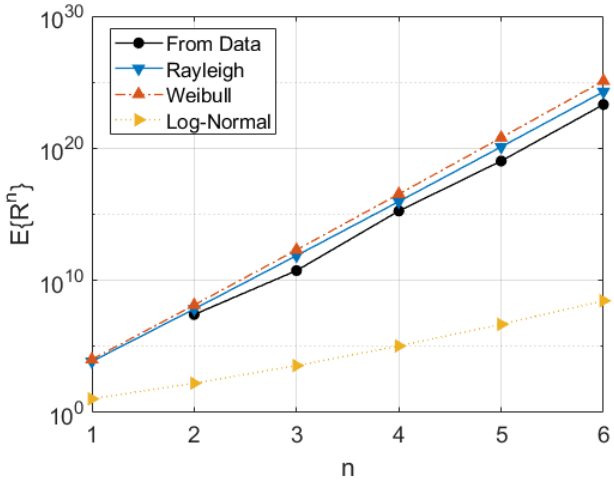

Fig. 10. Analysis of moments for TX_2-RX_2 radar channel at S-band at range cell no. 1067 (i.e., ≈ 400 m).

For the first case, i.e., the case of a monostatic radar channel, the analysis of the APDFs and their moments is reported in Fig. 9 and Fig. 10, respectively. Results demonstrate the strong similarity of the Rayleigh (blue line) and Weibull (red line) APDFs with the histogram obtained from the acquired data (black dots), especially in the first part of the density (i.e., the *bell*), see Fig. 9. Instead, the Log-Normal (yellow line) APDF is not accurate. This result is best demonstrated by the analysis of the moments, see Fig. 10.

For the second case, in which a bistatic radar channel is considered, the APDFs and their moments are reported in Fig. 11 and Fig. 12, respectively. The Weibull APDF fits apparently slightly better than the Rayleigh APDF the histogram obtained

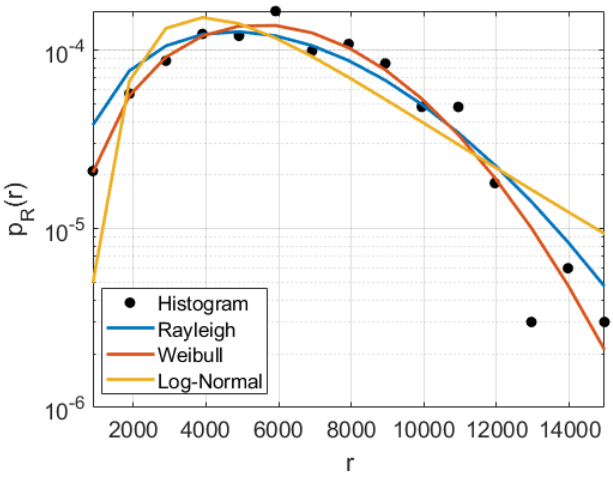

Fig. 11. Analysis of amplitude probability density functions (APDFs) for TX_2-RX_1 radar channel at S-band at range cell no. 2088 (i.e., $\approx$ 783 m).

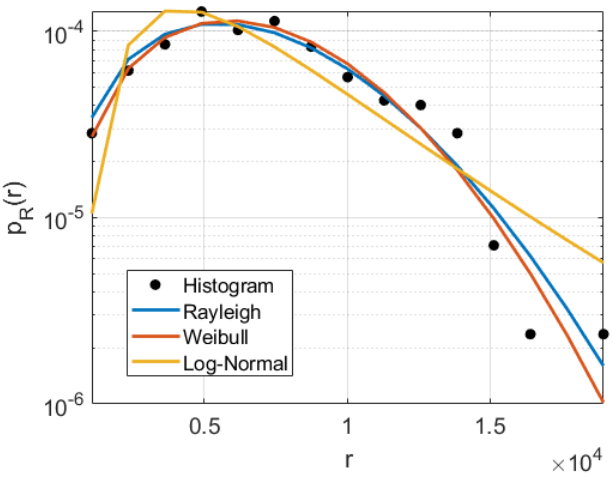

Fig. 13. Analysis of amplitude probability density functions (APDFs) for TX_2-RX_2 radar channel at X-band at range cell no. 1067 (i.e., $\approx$ 400 m).

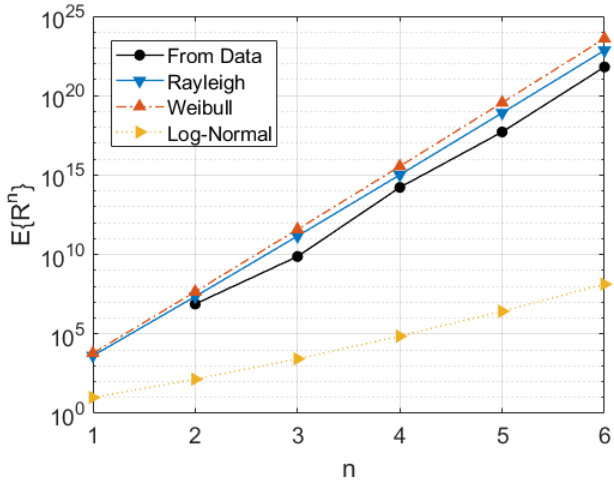

Fig. 12. Analysis of Moments for TX_2-RX_1 radar channel at S-band at range cell no. 2088 (i.e., $\approx$ 783 m).

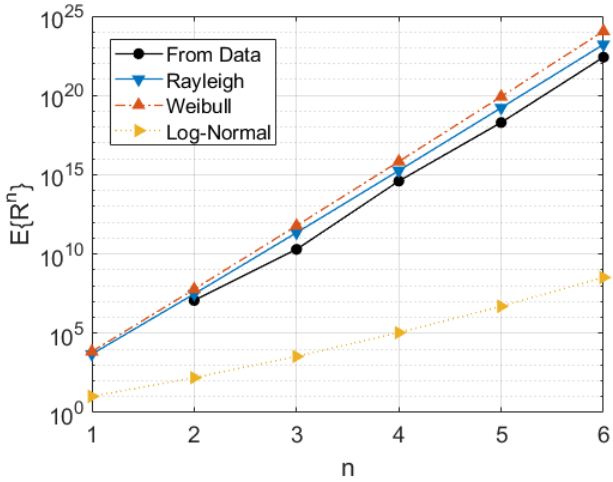

Fig. 14. Analysis of moments for TX_2-RX_2 radar channel at X-band at range cell no. 1067 (i.e., $\approx$ 400 m).

from the acquired data, see Fig. 11. Nevertheless, only with the analysis of the moments in Fig. 12, it is possible to understand that it is the Rayleigh distribution the one which provides a better fit of the empirical data at high-order moments.

Finally, as in the first case, the Log-Normal (yellow line) APDF does not provide a good fit of the data, as also corroborated by the analysis of the moments, see Fig. 12. Thus, it is possible to conclude that, at S-band and under very calm sea state conditions, at both monostatic and bistatic radar configurations, the best choice is the Rayleigh model, which not only provides a very good fit of the data, but also simplifies the mathematical tractability of the target detection problem.

2) X-band Radar Channels: The radar channel formed by TX_2 and RX_2 at X-band is analyzed at range cell no. 1067. The analysis of the APDFs and their moments is reported in Fig. 13 and Fig. 14, respectively. As for the S-band, although the strong similarity between the Rayleigh and Weibull APDFs, the best choice, from a mathematical tractability point of view is, again, the Rayleigh model.

Therefore, it is possible to conclude that the best choice for modelling sea clutter at both S- and X-bands, at both monostatic and bistatic radar configurations, in the considered application scenario (e.g., coarse azimuth resolution, not near grazing angle) is the Rayleigh distribution. In fact, this model not only provides a very good fit of the data, but also simplifies the mathematical tractability of the target detection problem.

However, it is worth noticing that this analysis has been conducted during summer, when the sea was very calm. Rough sea states, as well as the radar pointing direction with respect to the sea surface, i.e., the grazing angle, may lead to observe large *sea spikes* caused by breaking waves, as discussed in [13]. These conditions have an impact on the shorter or longer

tail of the APDF. Thus, it is not possible to conclude that the Rayleigh model would fit well the data also under different environmental and observation conditions.

Other well-known mathematical models are the K-distribution, the generalized K (GK) with Log-Normal texture and the GK with generalized Gamma texture, see [11], [13]. The GK models, which belong to the family of CG distributions are best suited to model heavy-tailed clutter distributions.

V. Conclusion

A detailed study of the statistical properties of sea clutter has been presented. The employed system is an innovative photonics-based dual-band coherent MIMO radar network with distributed antennas installed in the Port of Livorno, Italy. The system, which is integrated within the port monitoring infrastructure, employs in a coherent manner both monostatic and bistatic radar configurations, and it is capable of working at both S- and X-bands. The processed dataset was recorded on July 23, 2021, under very calm sea state conditions.

Skeweness and kurtosis coefficients have been calculated to evaluate the level of Gaussianity of the I amd Q signal components. The empirical distribution of the signal amplitude has been modelled using the Rayleigh, Weibull and Log-Normal distributions. Their scale and shape parameters have been estimated from the data samples using the method of moments.

Results of this analysis show that sea clutter can be modelled, at both monostatic and bistatic configurations, and in both bands as a complex Gaussian process, i.e., its amplitude is Rayleigh distributed. Although the Weibull model has provided very similar results, the Rayleigh model is to be preferred for its inherent simplicity in the mathematical tractability of the target detection problem. However, further acquisition campaigns, with the full-operating system, are necessary for validating the compound-Gaussian model in all sea state conditions.

Acknowledgment

The Authors would like to sincerely thank Prof. Maria Sabrina Greco, University of Pisa, Italy, for her valuable suggestions.

References

[1] V. S. Chernyak, Fundamentals of Multisite Radar System, London: Gordon & Breach Science Publ., 1998.

[2] A. M. Haimovich, R. S. Blum and L. J. Cimini, "MIMO Radar with Widely Separated Antennas," in IEEE Signal Processing Magazine, vol. 25, no. 1, pp. 116-129, 2008.

[3] G. Serafino, *et al.*, "Microwave Photonics for Remote Sensing: From Basic Concepts to High-Level Functionalities," in Journal of Lightwave Technology, vol. 38, no. 19, pp. 5339-5355, 1 Oct.1, 2020.

[4] S. Maresca, *et al.*, "Field Trial of a Coherent Widely Distributed Dual-Band Photonics-Based Radar Network in a Real Maritime Environment," 2021 Int. Top. Meet. on Microwave Photonics (MWP), 2021, pp. 1-4.

[5] G. Serafino, *et al.*, "A Photonics-Assisted Multi-Band MIMO Radar Network for the Port of the Future," in IEEE Journal of Selected Topics in Quantum Electronics, vol. 27, no. 6, pp. 1-13, Nov.-Dec. 2021.

[6] S. Maresca, *et al.*, "Field Trial of a Coherent, Widely Distributed, Dual-Band Photonics-Based MIMO Radar With ISAR Imaging Capabilities," in J. of Lightw. Tech., vol. 40, no. 20, pp. 6626-6635, 15 Oct.15, 2022.

[7] W. A. Al-Ashwal, *et al.*, "Analysis of bistatic sea clutter - Part I: Average reflectivity," in IEEE Trans. on Aerospace and Electronic Systems, vol. 50, no. 2, pp. 1283-1292, April 2014.

[8] W. A. Al-Ashwal, *et al.*, "Analysis of bistatic sea clutter - Part II: Amplitude statistics," in IEEE Trans. on Aerospace and Electronic Systems, vol. 50, no. 2, pp. 1293-1303, April 2014.

[9] R. Palamà, *et al.*, "Statistical analysis of bistatic and monostatic sea clutter," in IEEE Trans. on Aerospace and Electronic Systems, vol. 51, no. 4, pp. 3036-3054, Oct. 2015.

[10] M. Ritchie, *et al.*, "NetRAD: Monostatic and Bistatic Sea Clutter Texture and Doppler Spectra Characterization at S-Band," in IEEE Trans. on Geo. and Remote Sens., vol. 54, no. 9, pp. 5533-5543, Sept. 2016.

[11] S. Maresca, *et al.*, "The HF surface wave radar WERA. Part I: Statistical analysis of recorded data," 2010 IEEE Radar Conference, Arlington, VA, USA, 2010, pp. 826-831.

[12] S. Maresca, *et al.*, "The HF surface wave radar WERA. Part II: Spectral analysis of recorded data," 2010 IEEE Radar Conference, Arlington, VA, USA, 2010, pp. 969-974.

[13] M. Greco, F. Gini and M. Rangaswamy, "Statistical Analysis of Measured Polarimetric Clutter Data at Different Range Resolutions", IEE Proceedings on Radar Sonar Navigation, vol. 153, no. 6, pp. 473-481, December 2006.

[14] W. Huang, X. Liu, E. W. Gill, "Ocean Wind and Wave Measurements Using X-Band Marine Radar: A Comprehensive Review," Remote Sensing, 2017, 9, 1261, https://doi.org/10.3390/rs9121261.